This article has been accepted for inclusion in a future issue of this journal. Content is final as presented, with the exception of pagination.

Experimental Demonstration and Calibration of a 16-Element Active Incoherent Millimeter-Wave Imaging Array

Stavros Vakalis, *Student Member, IEEE*, Liang Gong, *Member, IEEE*, Yuxiao He, *Student Member, IEEE*, John Papapolymerou, *Fellow, IEEE*, and Jeffrey A. Nanzer, *Senior Member, IEEE*

***Abstract*— In this article, an active incoherent millimeter-wave imaging array is presented, along with its calibration procedure. Active incoherent millimeter-wave imaging uses the transmission of incoherent signals from multiple transmitters to mimic the properties of thermal radiation, enabling interferometric image reconstruction that can be realized in a snap-shot mode, without beamsteering. Due to the use of transmitters, the sensitivity requirement on the receivers is significantly relaxed compared with passive millimeter-wave imaging systems that detect low-power thermal radiation, making it possible to use standard commercial hardware, therefore decreasing the cost considerably. No exact knowledge of the transmit illumination is needed; thus, the coordination of the transmitters is minimal, further simplifying the system implementation. In this work, a 16-element K_a-band millimeter-wave imager is built and presented using commercial components and in-house fabricated antennas, along with a calibration procedure to account for amplitude and phase variations in the hardware. Experimental 2-D snapshot image reconstructions are presented.**

***Index Terms*— Calibration, distributed arrays, incoherent imaging, interferometric imaging, millimeter-wave imaging, noise radar, redundancy.**

I. Introduction

MICROWAVE and millimeter-wave imaging systems are attracting increasing interest for applications in remote sensing [1], security screening [2], [3], and medical imaging [4], [5], among others. Implementing such imagers in the millimeter-wave band can offer improved resolution and significantly more compact systems compared with microwave band implementations while maintaining good penetration through the fog, clouds, smoke, and clothing compared with optical and infrared imagers. The field of electromagnetic imaging is very active with a variety of techniques operating at frequencies ranging from a few GHz [6], [7] up to THz frequencies [8], [9]. Among the plethora of imaging techniques, staring techniques, which do not require mechanical or electrical scanning and, therefore, have good potential for real-time imaging, have attracted significant interest. Computational and compressive imagers can achieve staring image reconstruction with fewer samples than traditional imaging systems or fewer receive antenna elements [10]–[12] but are still limited by their heavy computational load, poor tolerance in low signal-to-noise ratio (SNR) scenarios, and the need for accurate knowledge of the transmit illumination. Passive interferometric imagers capture the inherently random thermal emissions from humans and other objects and have been developed to reconstruct the image by capturing samples in the spatial-frequency domain [13], [14]. First developed in radio astronomy [15], spatial-frequency sampling enables the generation of images using sparse antenna arrays in a staring configuration. In comparison with fully filled multielement phased arrays that collect samples in the spatial domain, a sparse array requires significantly fewer physical elements, reducing the cost and weight compared with phased arrays and mechanically steered systems. Also, compared with scanning techniques, which need to physically scan over the desired field of view, all antenna elements in an interferometric array simultaneously capture information corresponding to the entire image, thus forming images in a snap-shot mode, making them suitable for real-time applications.

Spatial-frequency sampling in interferometry relies on pairwise cross-correlations between a sparse set of antenna elements to reconstruct the image. Similar to an optical digital camera, the image reconstructions are produced without beam scanning or any mechanical moving parts. Since there is no direct mapping between each pixel and receiver, reconstructed images degrade gracefully with element failures, which increases the overall robustness and lifetime of the system. To employ the spatial-frequency image reconstruction method, the radiation from the scene must be incoherent in both space and time according to the Van Cittert–Zernike theorem [16]. Passive millimeter-wave imagers have been designed to create imagery out of the incoherent thermal emissions of the human body and other objects [17], [18]. However, in order to detect the extremely low-power thermal emissions, they require highly sensitive receivers with wide

Manuscript received November 22, 2019; revised January 31, 2020; accepted March 2, 2020. This work was supported by the National Science Foundation under Grant ECCS-1708820. *(Corresponding author: Jeffrey A. Nanzer.)*

Stavros Vakalis, Yuxiao He, John Papapolymerou, and Jeffrey A. Nanzer are with the Department of Electrical and Computer Engineering, Michigan State University, East Lansing, MI 48824 USA (email: vakaliss@msu.edu; nanzer@msu.edu).

Liang Gong was with the Department of Electrical and Computer Engineering, Michigan State University, East Lansing, MI 48824 USA. He is now with Amazon, Bellevue, WA 98004 USA.

Color versions of one or more of the figures in this article are available online at http://ieeexplore.ieee.org.

Digital Object Identifier 10.1109/TMTT.2020.2986413

bandwidth, which are costly and challenging to design and calibrate. Their integration time is also large, ranging from tens of milliseconds up to seconds.

Previous work has shown that illuminating the scene with multiple noise sources can mimic the properties of thermal radiation and produce microwave imagery [19]. By illuminating the scene with noise transmitters separated at a large number of wavelengths, the reflected radiation is both spatially and temporally incoherent, meeting the condition of the spatial-frequency image reconstruction and alleviating the high sensitivity requirement. Because of the higher SNR, bandwidth and integration time could be decreased by at least one order of magnitude compared with passive interferometric imaging systems [20]. Furthermore, no exact knowledge of the transmit field is needed, as long as it satisfies the incoherence requirement. Radar imaging techniques, such as frequency-modulated continuous-wave (FMCW) multiple-input multiple-output (MIMO) radar [21], [22], can also obtain imagery without analog beamscanning, but such techniques require precise knowledge of the transmitted waveform and also phase coherence between the transmitters. In comparison, active incoherent millimeter-wave imaging requires only knowledge of the statistics of the transmitted waveforms, and furthermore, the transmitters do not need to be phase-locked, simplifying the overall system complexity. Incoherent microwave imaging approaches have been attracting increasing interest lately due to the additional freedom that they can provide compared with the coherent counterparts [23]. More recently, the authors performed an experimental demonstration in the millimeter-wave band by synthesizing a 2-D array with only two antenna elements [24]. While synthesized measurements are important to show the feasibility of the technique and for initial system design, they do not take into account mutual coupling in an actual interferometric array, and variations in performance when multiple chains of RF hardware are used. In this article, we introduce the first active interferometric imaging array in the millimeter-wave band and a calibration method to correct variations in the hardware of the multielement array.

The main novelty of this article is summarized as follows.

1) We present the design and experimental validation of the first full 2-D 16-element active incoherent millimeter-wave imaging system with full receive array processing and image reconstruction. Prior works have shown only measured images generated by moving one or more elements to synthesize a 2-D array.
2) The first calibration procedure designed for active incoherent millimeter-wave imaging is presented and validated using a 37-GHz 16-element active incoherent imaging array. Importantly, this procedure does not require exact knowledge of the transmit waveforms; only the statistical properties need to be known. Furthermore, the calibration operates on a system level and does not require calibration of each channel individually, leading to a simpler, more direct calibration procedure.
3) Active incoherent millimeter-wave imaging achieves high sensitivity by illuminating the scene with incoherent radiation. Compared with passive imaging systems, sufficient sensitivity for fast image formation can, thus, be obtained with comparatively low-cost hardware. We demonstrate an active imaging system using commercial off-the-shelf hardware and printed antennas, leading to a low-cost overall millimeter-wave system.

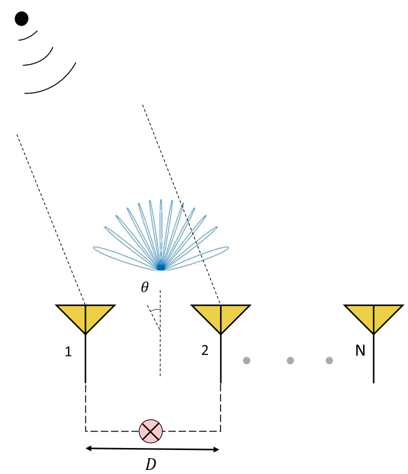

Fig. 1. Two elements of an interferometric array observing a radiating source. The blue fringe response corresponds to the correlation interferometer formed from antennas 1 and 2.

II. Active Incoherent Spatial-Frequency Sampling

Spatial-frequency sampling antenna arrays capture samples of the visibility $V(u,v)$, which is the spatial-frequency response of the scene given by the 2-D Fourier transform of the scene intensity $I(\alpha,\beta)$, where $\alpha = \sin\theta\cos\phi$ and $\beta = \sin\theta\sin\phi$ are the direction cosines relative to the azimuth and elevation planes. Each antenna pair in a correlator array corresponds to a specific spatial frequency, forming a point in the array's sampling function $S(u,v)$, and by cross-correlating the outputs of the antennas pairwise, a sample of the visibility is obtained for each antenna pair. For a given antenna pair with a baseline of D in an interferometric array, as shown in Fig. 1, the received signals from a radiating point source at each antenna can be given by [20], [25], [26]

$$V_1(t) = \cos(2\pi f_c t) + n_1(t) \tag{1}$$

$$V_2(t) = \cos[2\pi f_c(t-\tau_g)] + n_2(t) \tag{2}$$

where f_c is the carrier frequency, n_i is the noise generated by the ith receiver, and $\tau_g = D/c\sin\theta$ is the geometric time delay in which c is the speed of light and θ is the azimuth angle between the baseline D and the object scattering the illuminating signal. The two received signals are cross-correlated (multiplied and integrated), and because the signal voltage is incoherent with the noise components and the noise components are incoherent with each other, the noise components will average to zero as the integration time increases. The response of the correlation interferometer can then be given by

$$r(\theta) = \langle V_1 V_2\rangle = \big\langle\cos(2\pi f_c t)\cos[2\pi f_c(t-\tau_g)]\big\rangle. \tag{3}$$

Using a low-pass filter removes the high-frequency terms, resulting in

$$r(\theta) = \frac{1}{2}\cos\left(\frac{2\pi}{\lambda}D\sin\theta\right) \tag{4}$$

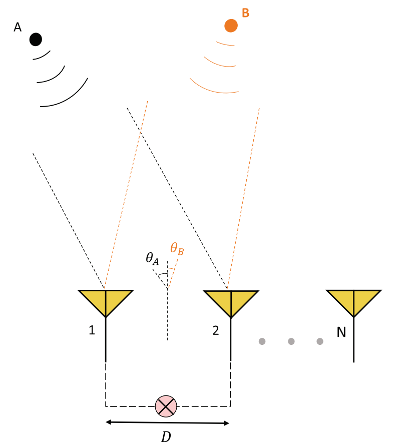

Fig. 2. Two elements of an interferometric array observing two radiating sources.

where $\lambda = c/f_c$ is the corresponding wavelength. The result is a fringe response with a number of sidelobes equal to the corresponding spatial frequency D/λ and can be seen in Fig. 1. In 2-D, the process of capturing spatial-frequency coefficients can be written in terms of the sampling function $S(u, v)$, which is multiplied with the scene visibility $V(u, v)$. The information captured by the array is the sampled visibility, which can be written as $V_s(u, v) = V(u, v) \cdot S(u, v)$. After capturing enough samples of these spatial-frequency distributed signals, the image is available through an inverse Fourier transform. This can be extended in 2-D as

$$I_r(\alpha, \beta) = \sum_n^N \sum_m^M V_s(u_n, v_m) e^{-j2\pi(u_n\alpha + v_m\beta)} \tag{5}$$

where I_r is the reconstructed image intensity and $N \cdot M$ is the maximum number of visibility samples. The spatial interpretation of this process can be seen from the point-spread function (PSF), which is the inverse Fourier transform of $S(u, v)$, using the duality between multiplication and convolution

$$I_r(\alpha, \beta) = \mathrm{PSF}(\alpha, \beta) * I(\alpha, \beta). \tag{6}$$

The PSF of an array usually consists of a main beam and a number of sidelobes.

The validity of the Fourier relationship between the visibility and the reconstructed intensity depends on the spatiotemporal coherence of $I(\alpha, \beta)$, according to the Van Cittert–Zernike theorem [16]. While thermal radiation emitted by objects conforms to this requirement, an active system must illuminate the scene with signals that are sufficiently incoherent in space and time to ensure a proper image reconstruction. A simple example to explain the difference between coherent and incoherent systems can be seen in the following. Consider an antenna baseline in the N-element interferometric array observing two point sources, as shown in Fig. 2. The two receiver voltages can be expressed as

$$V_1 = s_{1A} + s_{1B} + n_1 \tag{7}$$
$$V_2 = s_{2A} + s_{2B} + n_2 \tag{8}$$

where s_{iA} and s_{iB} are the terms that represent the response on the ith element due to the point sources A and B, respectively, and n_i is the noise received by the ith element. The output voltage, after cross-correlating the two receiver responses, can be given by

$$\begin{aligned} V_{out} &= \langle V_1 V_2 \rangle \\ &= \langle s_{1A} s_{2A} \rangle + \langle s_{1B} s_{2B} \rangle + \langle s_{1A} s_{2B} \rangle + \langle s_{1B} s_{2A} \rangle. \end{aligned} \tag{9}$$

Using traditional signal transmission, such as a continuous wave (CW) pulse, to illuminate the scene will result in a large correlation in the spatial domain. The correlation interferometer would not be able to capture only the visibility samples from the two targets, in this case, as the response would include unwanted cross-term information. This is the reason why previous work in interferometric imaging has taken place with passive systems that measure the thermally generated electromagnetic radiation. Thermal radiation is inherently noise-like, satisfying the incoherence requirement. In this article, we mimic the properties of thermal radiation by illuminating the scene with random noise-like signals that, when reflected and captured by the receiving array, are sufficiently uncorrelated in space and time to use the Fourier-based image reconstruction. The array of transmitters can, thus, be incoherent, requiring minimal coordination; the receiving array, however, must be coherent, as is the case with all interferometric imaging approaches.

Using an array of L noise transmitters, the response of the lth transmitter can be modeled as

$$x_l(t) = a_l(t) e^{j[2\pi f_c t + p_l(t)]} \tag{10}$$

where $a_l(t)$ and $p_l(t)$ are the Gaussian random amplitude and phase noise at the lth transmitter. In 1-D, at a much larger distance than the maximum dimension of the array, the spatiotemporal radiation from the incoherent transmit L-element array for narrow bandwidth Δf can be approximated as

$$A(\theta, t) = \sum_{l=1}^{L} x_l(t) \int_{f_c - \frac{1}{2}\Delta f}^{f_c + \frac{1}{2}\Delta f} e^{-j\frac{2\pi f}{c} d_l \sin\theta} df \tag{11}$$

where d_l represents the location of the lth transmitter in the array. By illuminating the scene in this way, each angular point obtains an incoherent response as a function of time. As a result, the signals from the point sources have very low correlation with each other, and the output voltage of the correlation interferometer can be expressed as

$$V_{\mathrm{out}} = \langle V_1 V_2 \rangle \approx \langle s_{1A} s_{2A} \rangle + \langle s_{1B} s_{2B} \rangle \tag{12}$$

where $\langle s_{1A} s_{2A} \rangle$ and $\langle s_{1B} s_{2B} \rangle$ represent the common parts from the two-point sources. In practice, the transmitted signals will be band limited and, thus, have some nonzero correlation. However, we have shown in previous work that even with a small correlation between the transmitted waveforms, image reconstruction can still take place [27], [28].

According to the Van Cittert–Zernike theorem, a distributed incoherent source will appear partially coherent when observed from a far enough distance from the receiver, i.e., two closely located incoherent emissions will start to appear to behave coherently due to the limited resolution of the receiver. A good practice for system design is, therefore, to set the maximum dimension of the transmit array to be larger than the maximum dimension of the receive array, such that any two points in

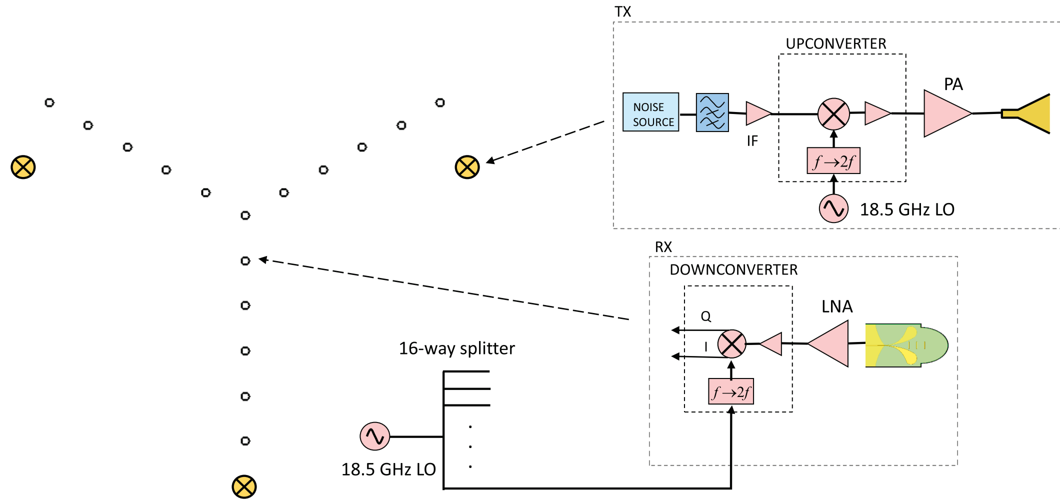

Fig. 3. 16-element active incoherent imaging system. 16 receivers (represented by white circles) are placed in the locations of a Y-array, and three transmitters are used (represented by the yellow circles with the crosses).

the scene that are separated by the resolution of the receiver or greater reflect incoherent radiation, therefore mitigating unwanted cross-product terms in the correlation interferometer response.

III. 16-Element Active Incoherent Imaging Array

In this section, the design of a sparse 16-element Y-shaped array is presented. A unique feature of this array apart from the noise illumination lies in the use of commercially available hardware.

A. Array System Design

The array configuration can be seen in Fig. 3. The three transmitters are represented by yellow circles with crosses, and the 16 receivers are represented by the smaller circles. The angle between the two arms of the Y-array is 120°. A Y-shaped formation was used because of its improved sampling function and field of view, due to hexagonal sampling [29], and the easy calibration procedure that can be applied to it, which will be discussed in Section IV.

A photograph of the imager can be seen in Fig. 4. The operating frequency of the imaging system was 37 GHz. The minimum distance between neighboring receive antenna elements in the Y-array was 24 mm (2.96 λ). The transmitters were three 0.2–2000-MHz low-cost baseband noise sources that were upconverted to 37 GHz. For a flatter noise response over the band of interest, a high-pass filter with a cutoff frequency of 20 MHz was used after each noise source, followed by a low-cost baseband amplifier of 30-dB gain that was, subsequently, fed into the intermediate frequency (IF) port of each upconverter. Three gallium arsenide (GaAs) monolithic microwave integrated circuit (MMIC) I/Q upconverters (Analog Devices HMC6787ALC5A) with integrated frequency doublers for the local oscillator (LO) inputs and a conversion gain of 10 dB each were used to mix the baseband noise to 37 GHz with an LO of 18.5 GHz. The 37-GHz noise signal was then boosted by three Analog Devices HMC7229LS6 power amplifiers, achieving approximately -10 dBm of maximum noise power at 37 GHz over a bandwidth of approximately 1 GHz.

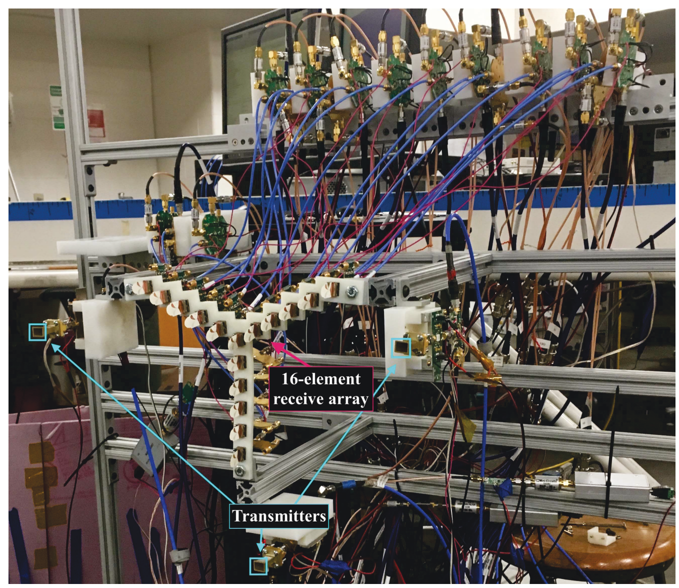

Fig. 4. Picture of the 16-element active incoherent imager. The three noise transmitters are separated at a larger spacing than the dimensions of the array.

For the receivers, each channel used a 9-dB printed Vivaldi antenna with an average measured S_{11} of -15 dB at 37 GHz. Each antenna was followed by a 20-dB gain Analog Devices HMC1040LP3CE low-noise amplifier (LNA) before being downconverted to baseband using a 37–44-GHz GaAs MMIC I/Q downconverter (Analog Devices HMC6789BLC5A). The inputs of the LNAs were directly connected to the end-launch connectors of the antennas, and the outputs were connected to the downconverters using 45.7-cm-long cables. The downconverted signals were captured using two 16-channel ATS9416 14-bit, 100-MS/s, AlazarTech waveform digitizers installed on a computer in master-slave mode. The sampling rate on the waveform digitizer was 100 MS/s, and the integration time was 20 μs, yielding a received signal bandwidth of 50 MHz. The signal processing was done in MATLAB. The Vivaldi antennas were fabricated in-house on a 2-mil liquid crystal polymer (LCP) substrate and are described in detail in [30]. Vivaldi antennas were chosen for this work due to their lower cost compared with standard gain horn antennas, and their compact and planar profile, which allows for shorter baselines in the interferometric array design. In addition, they offer high directivity, which can mitigate reflections outside the unambiguous field of view and boost the receive SNR. LCP was chosen because of its low-loss and flexibility [31].

The LO was distributed for the 16 receivers with two eight-way Mini-Circuits ZN8PD-02183-S+ splitters. 3-D printed structures were used to hold the 16 receive antennas in the correct positions. The Y-shaped 3-D printed structure had dimensions of 26 cm × 21 cm. The three transmitters were separated at a slightly larger separation than the largest antenna baseline in order to incoherently illuminate the scene at a finer spatial variation than the resolution of the receiving array to satisfy the incoherence requirement. Because the transmit pattern is not required to be known in general, there is significant freedom in the transmitter placement.

B. Array Spatial Resolution

The spatial resolution of a 2-D interferometric imager in the azimuth and elevation planes can be approximated with the null-to-null beamwidth θ_{NNBW} of the fringe response from the largest baselines in the horizontal and vertical axes of the array x and y [26]. This can be defined as

$$\Delta\theta_{\alpha,\beta} \approx \theta_{\mathrm{NNBW}}^{(\alpha,\beta)} \approx 2\frac{\lambda}{D_{x,y}} \quad . \tag{13}$$

While larger electrical baselines generally improve the resolution of the imaging system, capturing spatial-frequency samples using combinations of pairs in increments larger than $\lambda/2$ adds ambiguities and, therefore, decreases the unambiguous field of view. The half-angle unambiquous field of view of an interferometric imager with element spacings d_x and d_y across the horizontal and vertical axes can be expressed for the two direction cosines α and β as

$$\mathrm{FOV}_{\frac{\alpha}{2},\frac{\beta}{2}} = \frac{\lambda}{2 \cdot d_{x,y}}. \tag{14}$$

The PSF of the Y-array can be seen in Fig. 5, which shows that there are unwanted sidelobe responses in the edges of the field of view due to antenna spacings larger than $\lambda/2$. This can be tackled by multiplying the reconstructed image with a circular or a Gaussian beam to filter out the ghost responses on the edges of the image [29], [32]. In addition, directive antennas help mitigate the interference from outside the unambiguous field of view by focusing the radiated power broadside. The individual receive antenna radiation pattern can affect the PSF, which is the system's spatial response; however, directive antennas can be approximated to be uniform for the field of view close to broadside and for relatively narrow bandwidth. The difference in their complex gains (phase and amplitude) for the small field of view and narrow bandwidth will be calibrated in Section IV. The resolution of the imager was 4° and 5° in the azimuth and elevation planes, respectively. The corresponding unambiguous field of view due to the spacing increments was 22° and 38° in the azimuth and elevation planes.

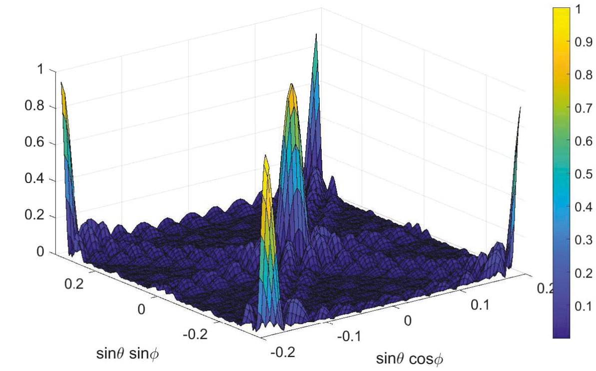

Fig. 5. Calculated PSF from the 16-element Y-array. Unwanted sidelobe behavior is encountered at the edges, which is expected from the Y-shaped array.

IV. Calibration Using Redundant Baselines

The use of off-the-shelf components has tremendous cost advantages compared with using customized components. However, such an approach makes the system more susceptible to uncertainties and variations in hardware performance. Interferometry can generally tolerate uncorrelated noise and small amplitude variations but is sensitive to phase variations between the different antenna elements. At 37 GHz, length variations on the order of millimeters represent a significant portion of the wavelength and, thus, a significant phase error. Apart from the in-house fabricated antennas, variations were found in the performance of the LNAs and downconverters. Also, the 18.5-GHz LO was fed after splitting by two eight-way splitters with 16 commercial cables, which produces small phase and amplitude unbalance, affecting the measured results.

The three noise transmitters need not be phase calibrated since their incoherence is necessary for the imaging operation as discussed in Section II. However, the large amplitude variations on the transmitters could be a problem because it could lead to the illuminating radiation being dominated by only one or two transmitters, reducing the spatial incoherence of the radiation. The low-cost noise sources used in this work had large amplitude variations; therefore, coaxial attenuators were used to match their output power at 37 GHz. After this calibration, the three transmitters had approximately the same power with variations smaller than 0.5 dB.

Many different techniques for calibrating interferometric receiving arrays in radio astronomy and remote sensing have been investigated [33]. Many of them rely on the knowledge of the scene that needs to be reconstructed or require some prior knowledge and an accurate model. To enable calibration of the array without knowledge of the scene, we implemented a calibration method using the redundant baselines of the Y-array. This method has also been studied in radio astronomy; however, its performance is poor in low-SNR conditions, resulting in calibration biases [34]. This can be a problem for passive interferometers when observing the thermal radiation from the sky or for a passive millimeter-wave imager when capturing the thermal emissions from a human. However, this work concerns an active system with signal illumination, meaning that high SNR can be easily achieved which minimizes the bias of the calibration.

In an interferometric array with N elements, the redundant baseline calibration can be described as follows [35]: consider the lth receiver element of the array, where $1 \le l \le N$, as shown in the bottom right of Fig. 3, to be represented by a complex gain G_l. Each measured visibility sample V_{lm}^{meas}, after cross-correlating the responses of the lth and mth elements, can be written as

$$V_{lm}^{\text{meas}} = V_{lm}^{\text{true}} G_l G_m^* + c_{lm} \tag{15}$$

where V_{lm}^{true} is the true visibility sample that the correlation interferometer is supposed to capture, and c_{lm} is an additive error that can be used to summarize the effects of undesired noise and other biases in the estimation. For a passive interferometer capturing thermal radiation, it is not always easy to neglect the c_{lm} terms, but, for an active system, it can be assumed that $V_{lm}^{\text{true}} G_l G_m^* \gg c_{lm}$. Then, (15) can be approximated as

$$V_{lm}^{\text{meas}} = V_{lm}^{\text{true}} G_l G_m^*. \tag{16}$$

In (16), the measured complex visibilities are the known quantities, and the true visibility samples and the complex gains of each receiver are the unknowns. The algorithm that we describe in the following solves for both the true visibility sample and complex gains of the receivers; however, only the complex gains are needed for the system calibration, while the true visibility samples are needed for image reconstruction; thus, for calibration purposes, the true visibility is arbitrary. After calibration, each receiver will be mapped to a complex gain, and the subsequent received signals can be directly calibrated prior to the image reconstruction.

By writing $V^{\text{meas}} = e^{(\upsilon + j\psi)}$ and $G = e^{(g+j\phi)}$ and taking the logarithm of (16), the gains and the phases can be separated as follows:

$$\upsilon_{lm}^{\text{meas}} = \upsilon_{lm}^{\text{true}} + g_l + g_m \tag{17}$$
$$\psi_{lm}^{\text{meas}} = \psi_{lm}^{\text{true}} + \phi_l - \phi_m. \tag{18}$$

Note that the phases need to be unwrapped in (18). The following additional constraints need to be added in order to solve (17) and (18):

$$\sum_l g_l = 0 \tag{19}$$
$$\sum_l \phi_l = 0. \tag{20}$$

One additional constraint for the phases is needed to introduce the geometry of the array and how the wavefront propagates, which is given by

$$\sum_l r_{x,l}\phi_l = 0 \tag{21}$$
$$\sum_l r_{y,l}\phi_l = 0 \tag{22}$$

where $\mathbf{r}_l = (r_{x,l}, r_{y,l})$ is the physical location of the lth antenna element. The next step is to identify the redundant baselines in the array, which are the ones that have the same vertical and horizontal spacing, and, therefore, capture the same information.

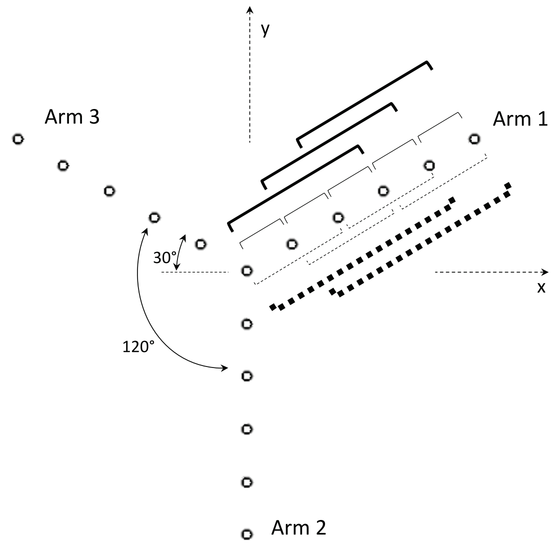

Fig. 6. Y-shaped array locations and redundant baselines on it. The same style line represents the redundant baseline pairs of the same spacing.

An example can be seen in Fig. 6, where the line style represents redundant baseline pairs that, according to interferometric processing, should measure the same complex visibility sample. Thus, the measurements taken by multiple redundant baselines of the same spacing can be compared with each other in order to determine the complex gains of each channel. Although they are only shown in arm 1 of the Y-shaped array, equivalent pairs can be found in the arms 2 and 3 of the array, and therefore, all receiver elements can be calibrated based on the redundancies of the information in each arm. Numbering the six elements in this arm 1, which is a linear array, from 1 to 6 starting from the top right of the figure, one can see that

$$V_{12}^{\text{true}} = V_{23}^{\text{true}} = V_{34}^{\text{true}} = V_{45}^{\text{true}} = V_{56}^{\text{true}} = V_1^{\text{true}}$$
$$V_{13}^{\text{true}} = V_{24}^{\text{true}} = V_{35}^{\text{true}} = V_{46}^{\text{true}} = V_2^{\text{true}}, \ldots$$

until all the redundant combinations are taken into account, where the single subscript indicates the difference in the relative positions of the antenna, and for simplicity, here, we show the linear array case of arm 1. The phases (18) can, thus, be written as (23), shown at the bottom of the next page. The second-to-last row represents the constraint from (20). The last row represents the constraints from (21) and (22). Only one row is needed for these two constraints because this particular subarray has $r_x = \cos(30°) \cdot [5\ \ 4\ \ 3\ \ 2\ \ 1\ \ 0]$ and $r_y = \sin(30°) \cdot [5\ \ 4\ \ 3\ \ 2\ \ 1\ \ 0]$, and the constants in the front can be simplified since the right-hand side is zero.

The least-squares solution of this problem $Ax = b$ can be found with $x = (A^TA)^{-1}A^Tb$. In order to calibrate all the 16 elements of the array, the matrix A should contain all the redundant information in the array for the three arms of the array. The element in the center should be present in the equations for the three arms in order to act as a reference and minimize differences in phase and amplitude between the three subarrays. The interaction between elements in different arms can be omitted because it does not provide redundancy in this particular case, and because the least-square estimation will try to solve for the true visibility samples, the problem can easily become ill-posed.

Initial simulations of this calibration method were run for the 16-element Y-array when observing a single point source. Each receive element was modeled with nonidealities by a complex gain $G = e^{(g+j\phi)}$. The amplitude variations g were uniformly distributed in the interval $[-0.5,\ 0.5]$, and the phase variations ϕ were uniformly distributed in the interval $\left[0,\ \pi\right]$. The uncalibrated point source reconstruction is shown in Fig. 7(a). The array observed the visibility of a single point source but produced a "dirty" beam, a term used in radio astronomy to describe when the sidelobe level is much higher than anticipated. The responses at the edges of the image caused by the PSF grating lobes (see Fig. 5) were filtered by multiplying the resulting image with a Gaussian window. After running the calibration algorithm using the redundancy in the baselines described in this section, the beam became much "cleaner," which can be seen in Fig. 7(b). The results indicate that in active systems where the SNR is not low, the redundant-baseline calibration approach can be applied even when the array does not have significant redundancy, such as the one presented in this article. In Section V, the algorithm will be applied to experimental data to compensate for the variations on the array that we discussed in section III.

V. Experimental Results

The first experimental measurements for this calibration were performed using a 30-dBsm trihedral corner reflector inside a semienclosed arch range to act as a strong point response. In Fig. 8, the uncalibrated dirty beam response can be seen on the top, while the calibrated beam response is shown on the bottom. The point-like response of the single reflector is clearly reconstructed after the calibration algorithm was applied. A Gaussian window was again applied to the image to remove the responses at the corners resulting from the grating lobes in the PSF. The least-squares calibration approach was implemented only once to determine the complex weights of each channel, after which the image formation procedure was implemented normally.

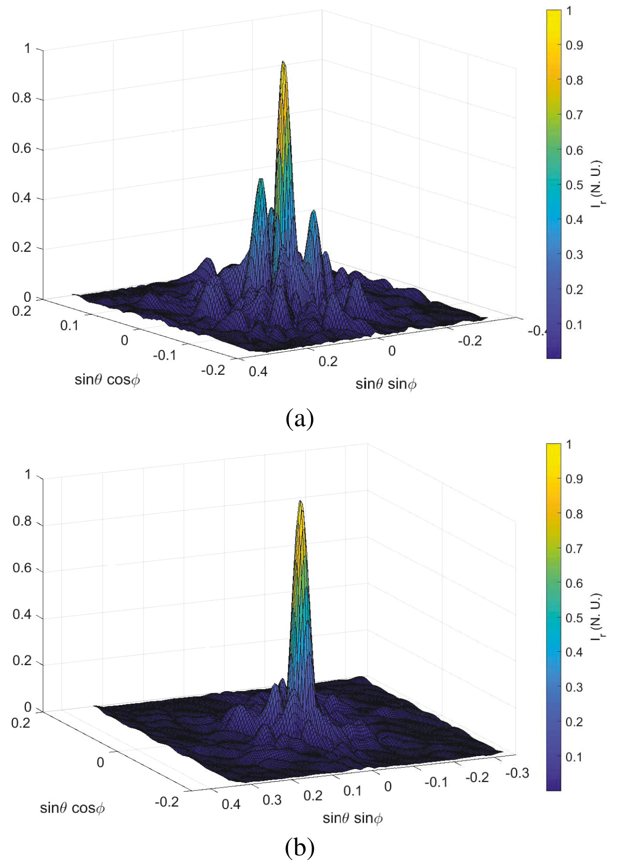

Fig. 7. (a) Simulated uncalibrated point source reconstruction from a 16-element Y-shaped array. (b) Simulated calibrated point source reconstruction using the redundant baselines in a 16-element Y-shaped array.

After the calibration, experimental measurements were taken inside a semienclosed arch range using a target comprised of two metal stripes on a foam board, as shown in Fig. 9. The two stripes were made with copper tape with dimensions of 38 cm × 10 cm, spaced vertically by 22 cm, and glued on the foam substrate. The target was placed inside the semienclosed arch range at a distance of 2.7 m away from the

$$\begin{pmatrix} 1 & -1 & 0 & 0 & 0 & 0 & 1 & 0 & 0 & 0 & 0 \\ 1 & 0 & -1 & 0 & 0 & 0 & 0 & 1 & 0 & 0 & 0 \\ 1 & 0 & 0 & -1 & 0 & 0 & 0 & 0 & 1 & 0 & 0 \\ 1 & 0 & 0 & 0 & -1 & 0 & 0 & 0 & 0 & 1 & 0 \\ 1 & 0 & 0 & 0 & 0 & -1 & 0 & 0 & 0 & 0 & 1 \\ 0 & 1 & -1 & 0 & 0 & 0 & 1 & 0 & 0 & 0 & 0 \\ 0 & 1 & 0 & -1 & 0 & 0 & 0 & 1 & 0 & 0 & 0 \\ 0 & 1 & 0 & 0 & -1 & 0 & 0 & 0 & 1 & 0 & 0 \\ 0 & 1 & 0 & 0 & 0 & -1 & 0 & 0 & 0 & 1 & 0 \\ 0 & 0 & 1 & -1 & 0 & 0 & 1 & 0 & 0 & 0 & 0 \\ 0 & 0 & 1 & 0 & -1 & 0 & 0 & 1 & 0 & 0 & 0 \\ 0 & 0 & 1 & 0 & 0 & -1 & 0 & 0 & 1 & 0 & 0 \\ 0 & 0 & 0 & 1 & -1 & 0 & 1 & 0 & 0 & 0 & 0 \\ 0 & 0 & 0 & 1 & 0 & -1 & 0 & 1 & 0 & 0 & 0 \\ 0 & 0 & 0 & 0 & 1 & -1 & 1 & 0 & 0 & 0 & 0 \\ 1 & 1 & 1 & 1 & 1 & 1 & 0 & 0 & 0 & 0 & 0 \\ 5 & 4 & 3 & 2 & 1 & 0 & 0 & 0 & 0 & 0 & 0 \end{pmatrix} \begin{pmatrix} \phi_1 \\ \phi_2 \\ \phi_3 \\ \phi_4 \\ \phi_5 \\ \phi_6 \\ \psi_1 \\ \psi_2 \\ \psi_3 \\ \psi_4 \\ \psi_5 \end{pmatrix} = \begin{pmatrix} \psi_{12} \\ \psi_{13} \\ \psi_{14} \\ \psi_{15} \\ \psi_{16} \\ \psi_{23} \\ \psi_{24} \\ \psi_{25} \\ \psi_{26} \\ \psi_{34} \\ \psi_{35} \\ \psi_{36} \\ \psi_{45} \\ \psi_{46} \\ \psi_{56} \\ 0 \\ 0 \end{pmatrix} \tag{23}$$

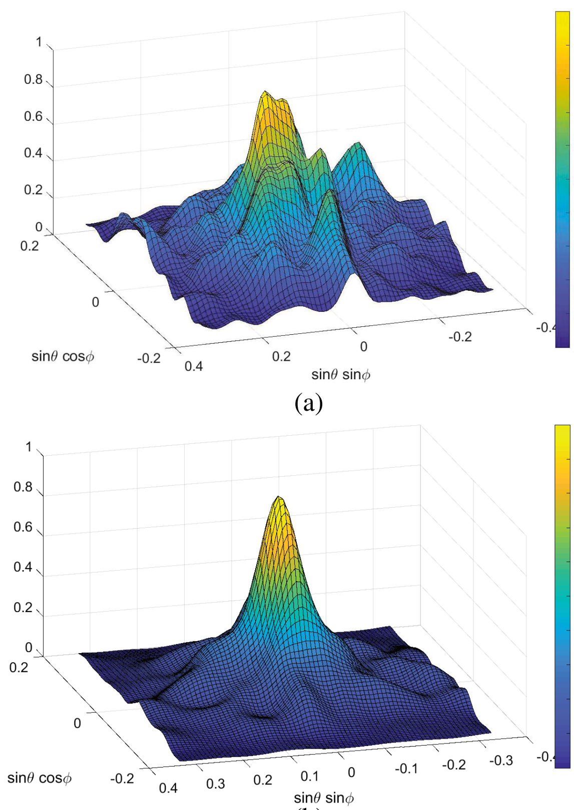

Fig. 8. (a) Experimental uncalibrated corner reflector reconstruction. (b) Experimental calibrated corner reflector reconstruction.

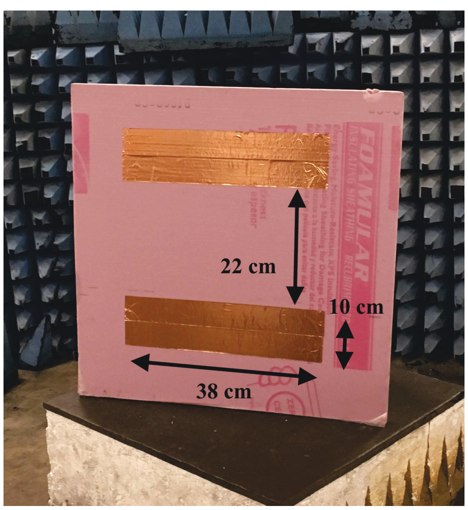

Fig. 9. Target consisting of two reflecting stripes from copper tape inside the semienclosed arch range.

imager; although this is in the near field of the receiving array, when located near broadside with the field of view used in this work, the phase errors are minimal compared with the far-field approximation [18], [36]. The uncalibrated reconstruction using the 37 GHz array can be seen in Fig. 10(a), showing clear inconsistencies compared with the target. The calibrated image reconstruction in Fig. 10(b) shows that the spurious responses prior to calibration have been successfully removed, resulting in two strong horizontal responses corresponding to the two metal stripes on the target. Good discrimination of the two responses can be seen from the imaging system.

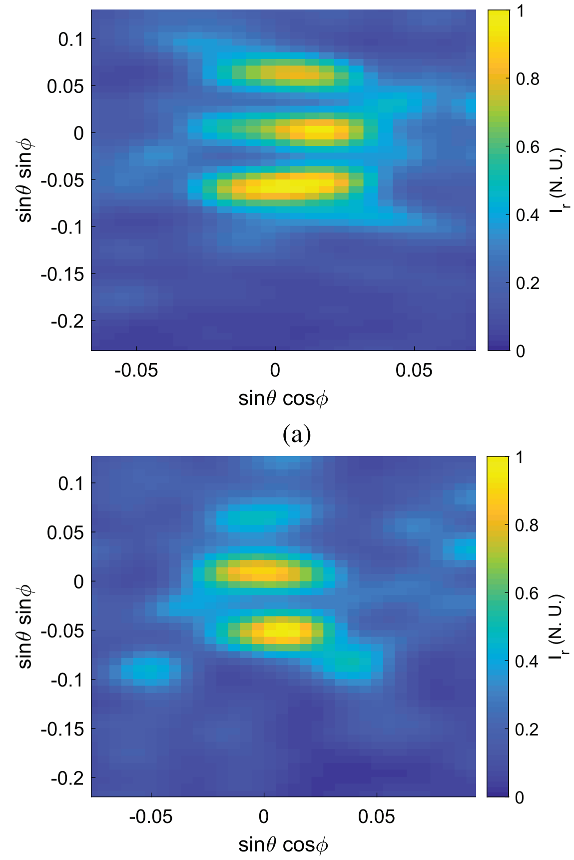

Fig. 10. (a) Experimental uncalibrated reconstruction of two reflecting stripes. (b) Experimental calibrated reconstruction of two reflecting stripes.

The responses are not as wide as the horizontal dimensions of the stripes because of the specularity of their reflections. The images were, furthermore, obtained with low computational complexity and using comparatively short integration time and bandwidth, each roughly an order of magnitude less than passive interferometric imagers [20].

VI. Conclusion

The first millimeter-wave active interferometric imaging array has been presented. Using the concept of spatial-frequency sampling and illuminating the scene with incoherent noise signals, we achieve a cost-effective solution with a sparse array and commercial components. A simple technique to compensate for hardware imperfections that leverage the good SNR afforded by active illumination was described. Good resolution and staring operation, along with very low computational complexity, show a very promising technique for real-time millimeter-wave imaging applications.

Acknowledgment

The authors would like to thank Brian Wright from Michigan State University for his help with the experimental setup.

References

[1] K. B. Cooper *et al.*, "Penetrating 3-D imaging at 4-and 25-m range using a submillimeter-wave radar," *IEEE Trans. Microw. Theory Techn.*, vol. 56, no. 12, pp. 2771–2778, Dec. 2008.

[2] R. Appleby and R. N. Anderton, "Millimeter-wave and submillimeter-wave imaging for security and surveillance," *Proc. IEEE*, vol. 95, no. 8, pp. 1683–1690, Aug. 2007.
[3] D. M. Sheen, D. L. Mcmakin, and T. E. Hall, "Three-dimensional millimeter-wave imaging for concealed weapon detection," *IEEE Trans. Microw. Theory Techn.*, vol. 49, no. 9, pp. 1581–1592, Sep. 2001.
[4] N. Nikolova, "Microwave imaging for breast cancer," *IEEE Microw. Mag.*, vol. 12, no. 7, pp. 78–94, Dec. 2011.
[5] E. J. Bond, X. Li, S. C. Hagness, and B. D. Van Veen, "Microwave imaging via space-time beamforming for early detection of breast cancer," *IEEE Trans. Antennas Propag.*, vol. 51, no. 8, pp. 1690–1705, Aug. 2003.
[6] Z. Peng *et al.*, "A portable FMCW interferometry radar with programmable low-IF architecture for localization, ISAR imaging, and vital sign tracking," *IEEE Trans. Microw. Theory Techn.*, vol. 65, no. 4, pp. 1334–1344, Apr. 2017.
[7] Y. Álvarez *et al.*, "Fourier-based imaging for multistatic radar systems," *IEEE Trans. Microw. Theory Techn.*, vol. 62, no. 8, pp. 1798–1810, Aug. 2014.
[8] K. B. Cooper, R. J. Dengler, N. Llombart, B. Thomas, G. Chattopadhyay, and P. H. Siegel, "THz imaging radar for standoff personnel screening," *IEEE Trans. THz Sci. Technol.*, vol. 1, no. 1, pp. 169–182, Sep. 2011.
[9] P. C. Theofanopoulos, M. Sakr, and G. C. Trichopoulos, "Multistatic terahertz imaging using the radon transform," *IEEE Trans. Antennas Propag.*, vol. 67, no. 4, pp. 2700–2709, Apr. 2019.
[10] J. Hunt *et al.*, "Metamaterial apertures for computational imaging," *Science*, vol. 339, no. 6117, pp. 310–313, Jan. 2013.
[11] T. Sleasman, M. Boyarsky, M. F. Imani, T. Fromenteze, J. N. Gollub, and D. R. Smith, "Single-frequency microwave imaging with dynamic metasurface apertures," *J. Opt. Soc. Amer. B, Opt. Phys.*, vol. 34, no. 8, p. 1713, Aug. 2017. [Online]. Available: http://josab.osa.org/abstract.cfm?URI=josab-34-8-1713
[12] T. Zhou *et al.*, "Microwave imaging customized on demand under random field illumination," *IEEE Trans. Microw. Theory Techn.*, vol. 67, no. 3, pp. 1148–1156, Mar. 2019.
[13] N. A. Salmon, I. Mason, P. Wilkinson, C. Taylor, and P. Scicluna, "First imagery generated by near-field real-time aperture synthesis passive millimetre wave imagers at 94 GHz and 183 GHz," in *Proc. Millimetre Wave THz Sensors Technol. III*, Oct. 2010, vol. 7837, no. 1, pp. 1–12.
[14] E. Kpre, C. Decroze, M. Mouhamadou, and T. Fromenteze, "Computational imaging for compressive synthetic aperture interferometric radiometer," *IEEE Trans. Antennas Propag.*, vol. 66, no. 10, pp. 5546–5557, Oct. 2018.
[15] A. R. Thompson, J. M. Moran, and G. W. Swenson, *Interferometry and Synthesis in Radio Astronomy*. Hoboken, NJ, USA: Wiley, 2001.
[16] M. Born and E. Wolf, *Principles of Optics*. Cambridge, U.K.: Cambridge Univ. Press, 1999.
[17] L. Yujiri, M. Shoucri, and P. Moffa, "Passive millimeter wave imaging," *IEEE Microw. Mag.*, vol. 4, no. 3, pp. 39–50, Sep. 2003.
[18] N. A. Salmon *et al.*, "First video rate imagery from a 32-channel 22-GHz aperture synthesis passive millimetre wave imager," in *Proc. Millimetre Wave THz Sensors Technol. IV*, Oct. 2011, vol. 8188, no. 5, pp. 1–12.
[19] S. Vakalis and J. A. Nanzer, "An active microwave imaging technique using spatial frequency sampling," in *IEEE MTT-S Int. Microw. Symp. Dig.*, Jun. 2018, pp. 816–818.
[20] S. Vakalis and J. A. Nanzer, "Microwave imaging using noise signals," *IEEE Trans. Microw. Theory Techn.*, vol. 66, no. 12, pp. 5842–5851, Dec. 2018.
[21] R. Feger, C. Wagner, S. Schuster, S. Scheiblhofer, H. Jager, and A. Stelzer, "A 77-GHz FMCW MIMO radar based on an SiGe single-chip transceiver," *IEEE Trans. Microw. Theory Techn.*, vol. 57, no. 5, pp. 1020–1035, May 2009.
[22] D. Bleh *et al.*, "W-band time-domain multiplexing FMCW MIMO radar for far-field 3-D imaging," *IEEE Trans. Microw. Theory Techn.*, vol. 65, no. 9, pp. 3474–3484, Sep. 2017.
[23] A. V. Diebold, M. F. Imani, T. Sleasman, and D. R. Smith, "Phaseless coherent and incoherent microwave ghost imaging with dynamic metasurface apertures," *Optica*, vol. 5, no. 12, pp. 1529–1541, Dec. 2018. [Online]. Available: http://www.osapublishing.org/optica/abstract.cfm?URI=optica-5-12-1529
[24] S. Vakalis, L. Gong, J. Papapolymerou, and J. Nanzer, "40-GHz active interferometric imaging with noise transmitters," in *Proc. Eur. Radar Conf. (EuRAD)*, Oct. 2019, pp. 273–276.
[25] J. A. Nanzer, *Microwave and Millimeter-Wave Remote Sensing for Security Applications*. Norwood, MA, USA: Artech House, 2012.
[26] S. Vakalis and J. A. Nanzer, "Analysis of array sparsity in active incoherent microwave imaging," *IEEE Geosci. Remote Sens. Lett.*, vol. 17, no. 1, pp. 57–61, Jan. 2020.
[27] S. Vakalis and J. A. Nanzer, "Transmit pattern analysis for active incoherent microwave imaging," in *Proc. IEEE Int. Symp. Antennas Propag. USNC-URSI Radio Sci. Meeting*, Jul. 2019, pp. 813–814.
[28] S. Vakalis, L. Gong, and J. A. Nanzer, "Imaging with WiFi," *IEEE Access*, vol. 7, pp. 28616–28624, 2019.
[29] A. Camps, J. Bara, I. C. Sanahuja, and F. Torres, "The processing of hexagonally sampled signals with standard rectangular techniques: Application to 2-D large aperture synthesis interferometric radiometers," *IEEE Trans. Geosci. Remote Sens.*, vol. 35, no. 1, pp. 183–190, Jan. 1997.
[30] Y. He and J. Papapolymerou, "Conformal antipodal Vivaldi antenna with parasitic elements for 5G millimeter wave applications," in *Proc. IEEE Int. Symp. Antennas Propag. USNC-URSI Radio Sci. Meeting*, Jul. 2019, pp. 271–272.
[31] D. C. Thompson, O. Tantot, H. Jallageas, G. E. Ponchak, M. M. Tentzeris, and J. Papapolymerou, "Characterization of liquid crystal polymer (LCP) material and transmission lines on LCP substrates from 30 to 110 GHz," *IEEE Trans. Microw. Theory Techn.*, vol. 52, no. 4, pp. 1343–1352, Apr. 2004.
[32] C. Zheng, X. Yao, A. Hu, and J. Miao, "A passive millimeter-wave imager used for concealed weapon detection," *Prog. Electromagn. Res. B*, vol. 46, pp. 379–397, 2013.
[33] A. B. Tanner and C. T. Swift, "Calibration of a synthetic aperture radiometer," *IEEE Trans. Geosci. Remote Sens.*, vol. 31, no. 1, pp. 257–267, Jan. 1993.
[34] A. Liu, M. Tegmark, S. Morrison, A. Lutomirski, and M. Zaldarriaga, "Precision calibration of radio interferometers using redundant baselines," *Monthly Notices Roy. Astronomical Soc.*, vol. 408, no. 2, pp. 1029–1050, Oct. 2010.
[35] M. H. Wieringa, "An investigation of the telescope based calibration methods 'redundancy' and 'self-cal,'" *Experim. Astron.*, vol. 2, no. 4, pp. 203–225, Jul. 1992. [Online]. Available: https://doi.org/10.1007/BF00420576
[36] J. A. Nanzer and R. L. Rogers, "A Ka-band correlation radiometer for human presence detection from a moving platform," in *IEEE MTT-S Int. Microw. Symp. Dig.*, Jun. 2007, pp. 385–388.

Stavros Vakalis (Student Member, IEEE) received the Diploma degree in electrical and computer engineering from the National Technical University of Athens, Athens, Greece, in 2017. He is currently pursuing the Ph.D. degree in electrical engineering at Michigan State University, East Lansing, MI, USA.

His current research interests include wireless microwave and millimeter-wave systems, millimeter-wave imaging, antenna arrays, and radar and signal processing.

Mr. Vakalis is also a member of the IEEE Microwave Theory and Techniques Society and the IEEE Antennas and Propagation Society. He received the Gerondelis Foundation Graduate Scholarship for his graduate studies. He has been serving as a Reviewer for the IEEE TRANSACTIONS ON MICROWAVE THEORY AND TECHNIQUES, the IEEE JOURNAL OF ELECTROMAGNETICS, RF AND MICROWAVES IN MEDICINE AND BIOLOGY, and the IEEE TRANSACTIONS ON ANTENNAS AND PROPAGATION.

Liang Gong (Member, IEEE) received the B.Eng. degree in electrical engineering from Xidian University, Xi'an, China, in 2008, and the M.Eng.Sc. and Ph.D. degrees from the Microsystems Research Group, School of Electrical Engineering and Telecommunications, University of New South Wales (UNSW), Sydney, NSW, Australia, in 2013 and 2017, respectively.

In 2012, he joined the Microsystems Research Group, School of Electrical Engineering and Telecommunications, UNSW. From 2018 to 2019, he was a Post-Doctoral Research Associate with the Department of Electrical and Computer Engineering, Michigan State University (MSU), East Lansing, MI, USA, jointly with UNSW. He is currently an Antenna Engineer with Amazon (Kuiper Project), Bellevue, WA, USA. His research interests include the RF MEMS, antennas, millimeter-wave circuits and systems, and radar and interferometric imaging systems.

Yuxiao He (Student Member, IEEE) received the B.S. degree in communications engineering from the Communication University of China, Beijing, China, in 2013, and the M.S. degree in electrical engineering from the University at Buffalo, The State University of New York, Buffalo, NY, USA, in 2016. He is currently pursuing the Ph.D. degree in electrical engineering at Michigan State University, East Lansing, MI, USA.

His current research interests include the design and fabrication of microwave and millimeter-wave circuits and antennas using additive manufacturing technologies, reconfigurable resonators and filters, and characterization and RF applications of nanomagnetic thin films.

Mr. He was a recipient of the Second Place Award of the Student Paper Competition at the 11th Global Symposium on Millimeter Waves, Boulder, CO, USA, in 2018.

John Papapolymerou (Fellow, IEEE) received the B.S.E.E. degree from the National Technical University of Athens, Athens, Greece, in 1993, and the M.S.E.E. and Ph.D. degrees from the University of Michigan, Ann Arbor, MI, USA, in 1994 and 1999, respectively.

From 1999 to 2001, he was an Assistant Professor with the Department of Electrical and Computer Engineering, The University of Arizona, Tucson, AZ, USA, and during the summers of 2000 and 2003, he was a Visiting Professor with the University of Limoges, Limoges, France. From 2001 to 2005, 2005 to 2009, and 2009 to 2013, he was an Assistant Professor, an Associate Professor, and a Professor, respectively, with the School of Electrical and Computer Engineering (ECE), Georgia Institute of Technology (Georgia Tech), Atlanta, GA, USA. From 2013 to 2015, he was the Ken Byers Professor with the School of ECE, Georgia Tech, and the Associate Director of the Georgia Electronic Design Center (GEDC) from 2011 to 2015. As of August 2015, he is the MSU Foundation Professor and the Chair of the Electrical and Computer Engineering Department, Michigan State University, East Lansing, MI, USA. He was selected as an MSU Academic Leadership Program (ALP) Fellow of the Big-Ten Academic Alliance during the 2018–2019 academic year. He has graduated 27 Ph.D. students and advised more than 50 post-doctoral fellows and graduate and undergraduate students throughout his career. He has authored or coauthored over 400 publications in peer-reviewed journals and conferences. He holds five U.S. patents. His research interests include the implementation of additive manufacturing technologies in the microwave, millimeter-wave and THz circuits, and the development of both passive and active planar circuits and antennas on semiconductor (Si/SiGe and GaAs), organic (LCP), and 3-D printed substrates for System-on-a-Chip (SOC)/System-on-a-Package (SOP) RF front ends.

Dr. Papapolymerou was a recipient of the 2012 IEEE Antennas and Propagation Society (AP-S) H. A. Wheeler Prize Paper Award, the 2010 IEEE AP-S John Kraus Antenna Award, the 2009 IEEE Microwave Theory and Techniques-Society (MTT-S) Outstanding Young Engineer Award, the 2009 Georgia Tech School of ECE Outstanding Junior Faculty Award, the 2004 Army Research Office (ARO) Young Investigator Award, the 2002 National Science Foundation (NSF) CAREER Award, the Best Paper Award at the 3rd IEEE International Conference on Microwave and Millimeter-Wave Technology (ICMMT2002), Beijing, China, and the 1997 Outstanding Graduate Student Instructional Assistant Award presented by the American Society for Engineering Education (ASEE), The University of Michigan Chapter. In 2004, he was the Chair of the IEEE MTT/AP Atlanta Chapter. He has served as the General Co-Chair of the 2019 IEEE International Symposium on Antennas and Propagation and the Editor-in-Chief of the IEEE MICROWAVE AND WIRELESS COMPONENTS LETTERS (MWCL) from 2012 to 2015. He has served as an Associate Editor for the IEEE TRANSACTIONS ON MICROWAVE THEORY AND TECHNIQUES from 2010 to 2012 and the Chair of the Commission D of the U.S. National Committee of URSI from 2009 to 2011. He was an Associate Editor for the IEEE MWCL from 2004 to 2007 and the IEEE TRANSACTIONS ON ANTENNAS AND PROPAGATION from 2004 to 2010.

Jeffrey A. Nanzer (Senior Member, IEEE) received the B.S. degrees in electrical engineering and in computer engineering from Michigan State University, East Lansing, MI, USA, in 2003, and the M.S. and Ph.D. degrees in electrical engineering from The University of Texas at Austin, Austin, TX, USA, in 2005 and 2008, respectively.

From 2008 to 2009, he was a Post-Doctoral Fellow with Applied Research Laboratories, The University of Texas at Austin, where he was involved in designing electrically small HF antennas and communication systems. From 2009 to 2016, he was with The Johns Hopkins University Applied Physics Laboratory, Laurel, MD, USA, where he created and led the Advanced Microwave and Millimeter-Wave Technology Section. In 2016, he joined the Department of Electrical and Computer Engineering, Michigan State University, where he is currently a Dennis P. Nyquist Assistant Professor. He has authored or coauthored more than 100 refereed journal articles and conference papers, authored *Microwave and Millimeter-Wave Remote Sensing for Security Applications* (Artech House, 2012), and coauthored the chapter "Photonics-Enabled Millimeter-Wave Wireless Systems" in *Wireless Transceiver Circuits* (Taylor & Francis, 2015). His current research interests include distributed arrays, radar and remote sensing, antennas, electromagnetics, and microwave photonics.

Dr. Nanzer is a member of the IEEE Antennas and Propagation Society Education Committee and the USNC/URSI Commission B. He was a Founding Member and the First Treasurer of the IEEE APS/ MTT-S Central Texas Chapter. He was a recipient of the Outstanding Young Engineer Award from the IEEE Microwave Theory and Techniques Society in 2019, the DARPA Director's Fellowship in 2019, the National Science Foundation (NSF) CAREER Award in 2018, the DARPA Young Faculty Award in 2017, and the JHU/APL Outstanding Professional Book Award in 2012. He has served as the Vice-Chair of the IEEE Antenna Standards Committee from 2013 to 2015. He was the Chair of the Microwave Systems Technical Committee (MTT-16), IEEE Microwave Theory and Techniques Society, from 2016 to 2018. He is also an Associate Editor of the IEEE TRANSACTIONS ON ANTENNAS AND PROPAGATION.